Acta Mech
https://doi.org/10.1007/s00707-024-04069-9

ORIGINAL PAPER

Sarabindu Dolui · **Ambalika Halder** · **Sharad Dwivedi**

Ultrafast domain wall motion in hexagonal magnetostrictive materials: role of inertial damping, magnetostriction, and dry-friction dissipation

Received: 29 September 2023 / Revised: 26 July 2024 / Accepted: 13 August 2024

Abstract This article investigates the dynamic features of domain walls in a bilayer piezoelectric-magnetostrictive heterostructure under the influence of piezo-induced strains, inertial damping, and dry friction dissipation. We assume that the magnetostrictive material belongs to the transversely isotropic hexagonal crystal. The analysis is carried out within the framework of the inertial Landau-Lifshitz-Gilbert equation, which describes the ultrafast evolution of magnetization inside the magnetostrictive materials. By employing the classical traveling wave ansatz, the study explores how various factors such as magnetoelasticity, dry friction, inertial damping, crystal symmetry, and a tunable external magnetic field characterize the motion of the magnetic domain walls in both steady-state and precessional dynamic regimes. The results present valuable insights into how these key parameters can effectively modulate dynamic features such as domain wall width, threshold, Walker breakdown, and domain wall velocity. The obtained analytical results are further numerically illustrated, and a qualitative comparison with recent observations is also presented.

Mathematics Subject Classification (2000) 35C07 · 35K55 · 35Q60 · 78A25 · 82D40

Abbreviations

DW	Domain wall
PES	Piezoelectric strip
FMS	Ferromagnetic strip
WB	Walker breakdown
MS	Magnetostrictive
iLLG	inertial Landau-Lifshitz-Gilbert

1 Introduction

Recent advances in materials science have led to a shift towards the development of hybrid magnetoelectric multiferroics for advanced applications in various fields such as electronics, medicine, automotive industry, aerospace, and robotics, among others (cf. [1–7]). One promising approach involves the creation of a mechanically coupled composite bilayer structure comprising a thin ferromagnetic strip (FMS) and a thick piezoelectric strip (PES), resulting in magnetoelastic effects that can significantly impact the magnetic domain wall (DW) motion. This strategic approach has the potential to revolutionize a wide spectrum of technologies, including

S. Dwivedi (✉) · S. Dolui · A. Halder
Department of Mathematics, School of Sciences, National Institute of Technology Andhra Pradesh, Tadepalligudem 534 101, India
E-mail: sharad@nitandhra.ac.in

Published online: 17 September 2024

energy harvesting, sensing, data storage, signal processing, spintronic devices, spin wave filters, transformers, actuators, and logic gates, opening up exciting possibilities for future innovations (cf. [1–8]). The success of these heterostructures relies on the possibility of achieving robust magnetoelectric coupling. In such composite structures, the synergy between magnetic and electric properties coexists and is coupled with each other.

Indeed, when a PES deforms upon the application of an electric field, it imposes strains on the FMS through the common surface. These piezo-induced strains are fully transferred to the FMS and substantially impact the magnetic state via inverse magnetostrictive effects (cf. [1,7,9–13]). Also, the crystal symmetry of the magnetic material plays a vital role since it affects anisotropy, magnetoelasticity, and magnetostrictive energies (cf. [7,13–16]). Ferromagnetic magnetostrictive materials that are often described in the literature include Co-Pt (platinum-cobalt alloys), Fe-Ga (Galfenol), $Tb_{1-x}Dy_xFe_2$ (terfenol-D), $NiFe_2O_4$, $CoFe_2O_4$, $BaFe_{12}O_{19}$ and various ferrites and manganites, whose lattice structures generally belong to the cubic or hexagonal crystal classes (cf. [7,14,17–20]). In particular, devices based on transversely isotropic ferromagnetic magnetostrictive materials are more advantageous due to their narrow DWs, stable magnetization states, and efficient current-induced DW motion. The present work focuses on a subclass of transversely isotropic hexagonal materials extensively used in modern DW-based devices.

It is observed that, in the presence of external stimuli, DW motion occurs in two dynamical regimes referred to as steady-state and precessional regimes. In the former dynamic regime, DW exhibits steady motion for the low-intensity applied magnetic field or electric current, sustaining a constant velocity across the major axis of the FMS. The maximum value of external sources for which DW motion remains steady is called the Walker breakdown (WB) limit, and the minimum value required to start DW motion is referred to as the depinning threshold. As the strength of the external stimulus surpasses the WB limit, the motion shifts into an oscillatory state due to internal deformation, known as precessional regime (cf. [7,10–12,21–24]).

Furthermore, the Landau-Lifshitz-Gilbert (LLG) equation is commonly used to describe the spatial and temporal changes in magnetization dynamics within the FMS (cf. [13,15,21,24–27]). Moreover, to understand the dissipative processes in materials with crystallographic defects (such as dislocations, impurities, and inclusions), the LLG equation has been extended, which includes a rate-independent dry-friction torque term, and the modified equation is called the Extended Landau-Lifshitz-Gilbert (ELLG) equation (cf. [7,12,23,28–30]). In addition, to accurately capture magnetization switching processes that occur on a very short timescale (ranging from sub-nanoseconds to sub-picoseconds), the ELLG equation is further augmented with an additional torque term referred to as inertial damping. This modified equation is known as the inertial Landau-Lifshitz-Gilbert equation (iLLG) (cf. [31–38]). This superimposed high-frequency inertial effects have been experimentally observed recently (cf. [37,39]). However, the inclusion of inertial term into the governing dynamics is theoretically well-established, whether through purely mechanical concepts or via the gyromagnetic relation linking the angular momentum (cf. [32–35,40]).

Contribution of the paper: This study aims to comprehensively examine the role of inertial damping in strain-induced DW motion in hybrid bilayer piezoelectric/magnetostrictive heterostructure under the influence of a tunable magnetic field. Recent works in the literature have focused on investigating DW motion in hybrid piezoelectric/magnetostrictive heterostructures across various crystal classes of magnetostrictive materials, such as cubic and hexagonal. These studies typically consider the FMS to be isotropic (cf. [21,41,42]), cubic (cf. [14,29,30]), or transversely isotropic hexagonal (cf. [1,7,12]). In addition, authors have also investigated the strain-mediated DW motion in a trilayer heterostructure consisting of a thick heavy metal, a thin ferromagnetic, and a metal oxide layer (cf. [1,43]). These investigations reveal that the interplay of key factors such as magnetostriction, crystal symmetry, and piezo-induced strain significantly impact the DW dynamics in bilayer and trilayer heterostructures and help to achieve larger DW velocities. Moreover, recent investigations have considered the inertial effects into the magnetization dynamics to investigate the ultrafast DW motion in ferromagnetic nanowires (cf. [31–37]). These investigations have revealed that incorporating inertial damping can substantially modulate DW properties, including velocity, depinning threshold, and breakdown, enabling faster and more energy-efficient data manipulation on very short timescales (cf. [2,10,31]).

However, a significant research gap remains as the effect of inertial damping has yet to be explored in analyzing the DW motion in such hybrid heterostructures. Also, the previous investigations predominantly focused on applying external stimuli in specific directions, leaving a need to comprehend how the anisotropic behavior of the material changes with respect to the direction of the field (cf. [12,21,23,29,30,38,44,45]). Therefore, in the present work, we make an earnest attempt to bridge these gaps. We present a comprehensive investigation of DW motion in hybrid piezoelectric/magnetostrictive heterostructures encompassing the simultaneous influence of an external magnetic field, inertial damping, strains, dry friction dissipation, magnetoelastic coupling, and magnetocrystalline anisotropy in both steady-state and precessional regimes. We utilize a tunable

magnetic field, allowing control over both direction and amplitude, to facilitate the impact of the external field orientation in the dynamics. Our investigation is based on the assumptions that ferromagnetic magnetostrictive material exhibits linear elasticity, the piezo-induced strains are spatially uniform and efficiently transferred from the PES to the FMS, and the external magnetic field's strength and direction can be tuned.

Structure of the paper In Sect. 2, we introduce a theoretical framework to investigate DW motion in a hybrid piezoelectric-magnetostrictive heterostructure employing a one-dimensional iLLG equation that governs DW motion in both steady and precessional regimes. Using the standard traveling wave ansatz, we derive the functional dependence of the most significant dynamical entities on the considered key parameters. Section 3 is dedicated to the numerical illustration of the analytical results obtained in the previous section. We characterize the DW motion in both dynamic regimes and provide a qualitative comparison with existing literature. Finally, Sect. 4 concludes this work with some plausible remarks.

2 The micromagnetic model

In this section, we analytically investigate the motion of magnetic DWs propagating along the major axis of a thin FMS affixed to the upper surface of a thick PES (cf. [7,12,14,21]), as illustrated in Fig. 1. We consider the dimensions of the FMS as L in length, w in width, and d in thickness along the $\mathbf{e}_1$, $\mathbf{e}_2$, and $\mathbf{e}_3$ directions, respectively. It is important to note that the physical setup adheres to the condition where the length greatly exceeds the width and thickness. Furthermore, the system is subjected to a constant in time and spatially uniform external magnetic field $\mathbf{h}_{\text{ext}}$, which can be oriented in any direction. Moreover, we assume that the external bias magnetic field $\mathbf{h}_{\text{ext}}$ controls the position of the domain wall, governing its motion along the major axis $\mathbf{e}_1$ of the FMS.

To analyze the one-dimensional motion of magnetic DWs along the major axis $\mathbf{e}_1$ of the nanostrip, we assume that all relevant physical parameters depend functionally on both time t and the major axis coordinate x (denotes the position along the FMS). In literature, this method is well-adopted for modeling DW dynamics in thin and elongated geometries (cf. [7,12,14,21,23,29,42]). In our analysis, we account for the following factors influencing the DW motion: the effects arising from the exchange interactions, magnetocrystalline anisotropy, stress-free magnetostriction, and magnetoelastic fields. Furthermore, when subjected to an electric voltage imposed between two lateral electrodes, the PES undergoes deformation, which further induces an electric field acting along the $\mathbf{e}_2$-axis. This, in turn, causes the PES width to elongate (or contract) along the same $\mathbf{e}_2$-axis while simultaneously causing contraction (or elongation) in the other two perpendicular directions. The strains generated in the PES are fully moved to the FMS through the shared interface due to strong acoustic contact between the two strips. Since the FMS is comparatively thinner than the PES, its mechanical properties are disregarded.

The spatiotemporal evolution of the magnetization vector inside the FMS, accounting for inertial and nonlinear dissipative effects, is governed by the iLLG equation (cf. [31–38]):

$$\dot{\mathbf{m}} = \mathbf{t}^{\text{prec}} + \mathbf{t}^{\text{dis}} + \mathbf{t}^{\text{iner}}, \tag{2.1}$$

where, $\mathbf{m} : \mathbb{R} \times \mathbb{R}^+ \to \mathbb{S}^2$ represents the normalized magnetization vector given by $\mathbf{m}(x,t) = \mathbf{M}(x,t)/M_s$. Also, $\mathbf{M}(x,t)$ represents the magnetization vector field, M_s denotes the saturation magnetization, and $\mathbb{S}^2$ corresponds to the unit sphere in $\mathbb{R}^3$. The variables x and t represent the spatial and temporal dimensions, respectively. In addition, $\mathbf{t}^{\text{prec}}$, $\mathbf{t}^{\text{dis}}$, and $\mathbf{t}^{\text{iner}}$ correspond to the precessional, dissipation, and inertial damping torque terms, respectively.

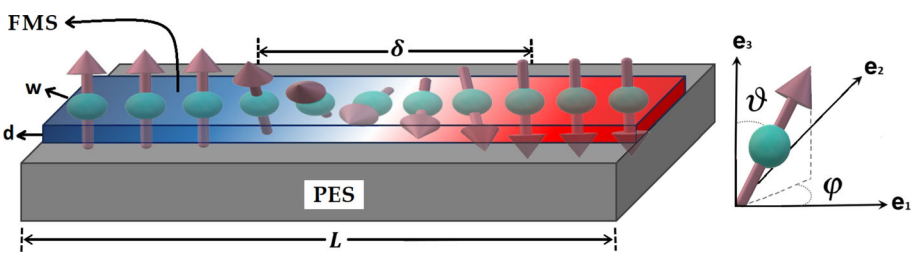

Fig. 1 Diagram of a bilayer composite structure consisting of ferromagnetic and piezoelectric strips together with the frame of reference

Now, we elucidate each torque component in the right-hand side of Eq. (2.1). The initial term corresponds to undamped precession, resulting in the magnetic moment's rotation around the direction of the total effective field $\mathbf{h}_{\text{eff}}$ and reads as:

$$\mathbf{t}^{\text{prec}} = -\gamma\ (\mathbf{m} \times \mathbf{h}_{\text{eff}}), \tag{2.2}$$

where, the constant γ is defined as $\gamma = M_s \mu_0 \gamma_e$, μ_0 represents the magnetic permeability of vacuum, and $\gamma_e = ge/m_e$, being g the Landè factor, e the charge of an electron, and m_e the electron mass. The total effective field $\mathbf{h}_{\text{eff}}$, which include the contribution of exchange $\mathbf{h}_{\text{ex}}$, demagnetization $\mathbf{h}_{\text{dmg}}$, magnetocrystalline anisotropy $\mathbf{h}_{\text{an}}$, magnetoelastic $\mathbf{h}_{\text{me}}$ and external magnetic $\mathbf{h}_{\text{ext}}$ fields and given as:

$$\mathbf{h}_{\text{eff}} = \mathbf{h}_{\text{ex}} + \mathbf{h}_{\text{dmg}} + \mathbf{h}_{\text{an}} + \mathbf{h}_{\text{me}} + \mathbf{h}_{\text{ext}}. \tag{2.3}$$

The exchange field $\mathbf{h}_{\text{ex}}$, which is responsible for aligning neighboring magnetic dipole moments parallel to each other, can be expressed as (cf. [12,14,23,29,30]):

$$\mathbf{h}_{\text{ex}} = A \frac{\partial^2 \mathbf{m}}{\partial x^2}, \tag{2.4}$$

where the constant $A = 2A_{\text{exc}}/(\mu_0 M_s^2)$, A_{exc} represents the exchange stiffness constant, which relies on material characteristics like crystal structure, electron configuration, and atomic spacing.

The demagnetizing field $\mathbf{h}_{\text{dmg}}$ can be approximated as (cf. [12,14,23,29]):

$$\mathbf{h}_{\text{dmg}} = -N_1 m_1 \mathbf{e}_1 - N_2 m_2 \mathbf{e}_2 - N_3 m_3 \mathbf{e}_3, \tag{2.5}$$

where N_1, N_2, and N_3 represent demagnetizing factors, which are influenced by the shape and geometry of the ferromagnetic material, and satisfy the normalization condition $N_1 + N_2 + N_3 = 1$. Determining the demagnetizing field involves complex calculations and typically requires numerical evaluations. However, for certain favorable geometries, such as a uniformly magnetized ellipsoid, a parallelepiped, and a straight nanowire with a circular cross-section, explicit expressions for the demagnetizing field can be derived (cf. [10,24,25,46–51]). For non-ellipsoidal geometries, such as thin films and nanostrips, the expression (2.5) for the demagnetizing field $\mathbf{h}_{\text{dmg}}$ is widely used in the literature as a reliable approximation (cf. [12,14,23,28–31,42]).

In contrast to cubic crystals, hexagonal crystals exhibit a distinctive behavior in the magnetocrystalline anisotropy field due to their lower degree of symmetry, resulting in energetically preferred magnetization directions. Moreover, hexagonal crystals possess a basal plane characterized by a high degree of symmetry, and the magnetization rotates more readily within this plane than perpendicular to it (cf. [52,53]). To be precise, for the considered hexagonal crystal classes with the easy axis direction $\mathbf{e}_3$, the magnetocrystalline anisotropy field takes the form (cf. [1,7,14,30,54]):

$$\mathbf{h}_{\text{an}} = \frac{2K}{\mu_0 M_s^2} (\mathbf{m} \cdot \mathbf{e}_3)\ \mathbf{e}_3, \tag{2.6}$$

where, K is the uniaxial anisotropy coefficient.

The magnetoelastic field $\mathbf{h}_{\text{me}}$ of a hexagonal crystal ferromagnetic material comprising both elastic and magnetostrictive strains can be expressed as follows (cf. [7,12–14]):

$$\mathbf{h}_{\text{me}} = \frac{1}{\mu_0 M_s^2} (\boldsymbol{\epsilon} - \boldsymbol{\epsilon}^{\text{m}}) : \mathbb{C} : \frac{\partial \boldsymbol{\epsilon}^{\text{m}}}{\partial \mathbf{m}}, \tag{2.7}$$

where, $\boldsymbol{\epsilon} = \boldsymbol{\epsilon}^e + \boldsymbol{\epsilon}^{\text{m}}$, $\boldsymbol{\epsilon}^e$ denotes the total elastic strain and $\boldsymbol{\epsilon}^{\text{m}} = \mathbb{Z} : (\mathbf{m} \otimes \mathbf{m})$ represents the magnetostrictive strain. Moreover, ":", $\mathbb{C}$, "$\otimes$" and $\mathbb{Z}$ correspond to the double contraction, elasticity tensors, tensor product, and fourth-order magnetostriction tensor, respectively. Eq. (2.7) reveals that the symmetry of the crystal affects the magnetoelastic field via the elasticity tensor $\mathbb{C}$ and the magnetostriction tensor $\mathbb{Z}$ through the magnetostrictive strain tensor $\boldsymbol{\epsilon}^{\text{m}}$.

In Voigt's compact notation, the elasticity tensor $\mathbb{C}$ can be represented as a 6×6 matrix. In the case of hexagonal crystal classes such as $\bar{6}$m2, 6mm, 622, and 6/mmm that exhibit transverse isotropy, delineating an

invariance under rotations about a specific axis of symmetry (chosen as $\mathbf{e}_3$ in our analysis), the elasticity tensor $\mathbb{C}$ can be expressed using five independent elastic constants as follows:

$$[\mathbf{C}] = \begin{bmatrix} c_{11} & c_{12} & c_{13} & & & \\ c_{12} & c_{11} & c_{13} & & \mathbf{0} & \\ c_{13} & c_{13} & c_{33} & & & \\ & & & c_{44} & 0 & 0 \\ & \mathbf{0} & & 0 & c_{44} & 0 \\ & & & 0 & 0 & \dfrac{c_{11}-c_{12}}{2} \end{bmatrix}. \tag{2.8}$$

For transversely isotropic hexagonal crystals, the fourth-order magnetostriction tensor $\mathbb{Z}$ can be expressed using six independent magnetostriction coefficients and can be written as follows:

$$[Z] = \begin{bmatrix} Z_{1111} & Z_{1122} & Z_{1133} & & & \\ Z_{1122} & Z_{1111} & Z_{1133} & & \mathbf{0} & \\ Z_{3311} & Z_{3311} & Z_{3333} & & & \\ & & & Z_{2323} & 0 & 0 \\ & \mathbf{0} & & 0 & Z_{2323} & 0 \\ & & & 0 & 0 & \dfrac{1}{2}(Z_{1111}-Z_{1122}) \end{bmatrix}. \tag{2.9}$$

Using Eq. (2.9), the magnetostriction strain tensor $\boldsymbol{\epsilon}^{\mathrm{m}}$ takes the following form (cf. [7,53–55]):

$$[\epsilon^{\mathrm{m}}] = \begin{bmatrix} Z_{1111}m_1^2 + Z_{1122}m_2^2 + Z_{1133}m_3^2 & (Z_{1111}-Z_{1122})m_1m_2 & 2Z_{2323}m_1m_3 \\ (Z_{1111}-Z_{1122})m_1m_2 & Z_{1122}m_1^2 + Z_{1111}m_2^2 + Z_{1133}m_3^2 & 2Z_{2323}m_2m_3 \\ 2Z_{2323}m_1m_3 & 2Z_{2323}m_2m_3 & Z_{3311}m_1^2 + Z_{3311}m_2^2 + Z_{3333}m_3^2 \end{bmatrix}. \tag{2.10}$$

By considering the differential value of $\boldsymbol{\epsilon}^{\mathrm{m}}$ measured with respect to the configuration in which the material is magnetized along its easy axis (in our analysis, we set $\mathbf{e}_3$), and the differential of scalar magnetostriction $\lambda_{\mathbf{n}}$, Eq. (2.10) can be rewritten as follows (cf. [7,12,55,56]):

$$[\boldsymbol{\epsilon}^{\mathrm{m}}] = \begin{bmatrix} (\lambda_A-\lambda_B)m_1^2 - \lambda_B m_3^2 + \lambda_B + \lambda_{13} & (\lambda_A-\lambda_B)m_1m_2 & \lambda_E m_1m_3 \\ (\lambda_A-\lambda_B)m_1m_2 & (\lambda_A-\lambda_B)m_2^2 - \lambda_B m_3^2 + \lambda_B + \lambda_{13} & \lambda_E m_2m_3 \\ \lambda_E m_1m_3 & \lambda_E m_2m_3 & \lambda_C(1-m_3^2) + \lambda_{33} \end{bmatrix}. \tag{2.11}$$

where, the scalar strains, $\lambda_A = Z_{1111} - Z_{1133}$, $\lambda_B = Z_{1122} - Z_{1133}$, $\lambda_C = Z_{3311} - Z_{3333}$, $\lambda_E = 2Z_{2323}$, $\lambda_{13} = Z_{1133}$, and $\lambda_{33} = Z_{3333}$.

By virtue of Eq. (2.11), the components of the magnetoelastic field can be derived and expressed as:

$$\begin{aligned} h_1^{\mathrm{me}} = \frac{2}{\mu_0 M_s^2}\Big\{ & (\lambda_A-\lambda_B)\,m_1\Big[c_{11}\Big(\epsilon_{11} - (\lambda_A-\lambda_B)\,m_1^2 + \lambda_B m_3^2 - (\lambda_B+\lambda_{13})\Big) \\ & + c_{12}\Big(\epsilon_{22} - (\lambda_A-\lambda_B)\,m_2^2 + \lambda_B m_3^2 - (\lambda_B+\lambda_{13})\Big) + c_{13}\Big(\epsilon_{33} + \lambda_C m_3^2 - (\lambda_C+\lambda_{33})\Big)\Big] \\ & + 2c_{44}\Big(\epsilon_{13} - \lambda_E m_1 m_3\Big)\lambda_E m_3 + \Big(c_{11}-c_{12}\Big)\Big(\epsilon_{12} - (\lambda_A-\lambda_B)\,m_1m_2\Big)\Big(\lambda_A-\lambda_B\Big)m_2\Big\}, \end{aligned}$$

$$
\begin{aligned}
h_2^{\mathrm{me}} = \frac{2}{\mu_0 M_s^2}\Big\{ & (\lambda_A-\lambda_B)\, m_2\Big[c_{12}\Big(\epsilon_{11}-(\lambda_A-\lambda_B)\, m_1^2+\lambda_B m_3^2-(\lambda_B+\lambda_{13})\Big)\\
& +c_{11}\Big(\epsilon_{22}-(\lambda_A-\lambda_B)\, m_2^2+\lambda_B m_3^2-(\lambda_B+\lambda_{13})\Big)+c_{13}\Big(\epsilon_{33}+\lambda_C m_3^2-(\lambda_C+\lambda_{33})\Big)\Big]\\
& +2c_{44}\Big(\epsilon_{23}-\lambda_E m_2 m_3\Big)\lambda_E m_3+\Big(c_{11}-c_{12}\Big)\Big(\epsilon_{12}-(\lambda_A-\lambda_B)\, m_1 m_2\Big)\Big(\lambda_A-\lambda_B\Big)m_1\Big\},\\
h_3^{\mathrm{me}} = \frac{2}{\mu_0 M_s^2}\Big\{ & -\lambda_B m_3\Big[(c_{11}+c_{12})\Big(\epsilon_{11}+\epsilon_{22}-(\lambda_A-\lambda_B)\left(m_1^2+m_2^2\right)+2\lambda_B m_3^2-2\,(\lambda_B+\lambda_{13})\Big)\\
& +2c_{13}\Big(\epsilon_{33}+\lambda_C m_3^2-\lambda_C-\lambda_{33}\Big)\Big]-\lambda_C m_3\Big[c_{13}\Big(\epsilon_{11}+\epsilon_{22}-(\lambda_A-\lambda_B)\left(m_1^2+m_2^2\right)+2\lambda_B m_3^2\\
& -2\,(\lambda_B+\lambda_{13})\Big)+c_{33}\Big(\epsilon_{33}+\lambda_C m_3^2-\lambda_C-\lambda_{33}\Big)\Big]+2c_{44}\lambda_E\Big(\,(\epsilon_{23}-\lambda_E m_2 m_3)\, m_2\\
& +(\epsilon_{13}-\lambda_E m_1 m_3)\, m_1\Big)\Big\}.
\end{aligned}
\tag{2.12}
$$

To properly determine the magnetoelastic field $\mathbf{h}_{\mathrm{me}}$, it is necessary to specify the values of the six independent components (ϵ_{11}, ϵ_{22}, ϵ_{33}, ϵ_{12}, ϵ_{13}, and ϵ_{23}) of the total strain $\boldsymbol{\epsilon}$. Given the thinner geometry of FMS, it is justifiable to disregard any strain variations along the $\mathbf{e}_3$ direction. Therefore, to characterize the total strains experienced by the FMS in the proposed composite structure, mechanical boundary conditions must be applied to both the upper and lower surfaces ($\mathbf{e_1}$-$\mathbf{e_2}$ plane) of the FMS. It is plausible to assume that the thicker PES imposes the magnetization-independent planar strains ϵ_{11}, ϵ_{12}, and ϵ_{22} on the FMS, since the lower surface of the thin FMS is perfectly attached to the thick PES. Also, the non-zero planar strains ϵ_{11} and ϵ_{22} are related via the Poisson ratio $\boldsymbol{\nu}$ (cf. [7,12,21,29]). Furthermore, the estimation of the remaining strain tensor components is evaluated by applying traction boundary conditions $\boldsymbol{\sigma}\mathbf{n} = \mathbf{0}$ at the top surface of the FMS. Here, $\boldsymbol{\sigma} = \mathbb{C} : (\boldsymbol{\epsilon} - \boldsymbol{\epsilon}^{\mathrm{m}})$ represents the Cauchy stress tensor, and $\mathbf{n} \equiv \mathbf{e}_3$ represents the normal vector to the top surface, rendering the following constraints:

$$
\begin{cases}
\sigma_{13} = 0 \Rightarrow \epsilon_{13} = \lambda_E m_1 m_3, \\
\sigma_{23} = 0 \Rightarrow \epsilon_{23} = \lambda_E m_2 m_3, \\
\sigma_{33} = 0 \Rightarrow \epsilon_{33} = \frac{c_{13}}{c_{33}}[(\lambda_A+\lambda_B)(1-m_3^2)+2\lambda_{13}-(\epsilon_{11}+\epsilon_{22})]+\lambda_C(1-m_3^2)+\lambda_{33}.
\end{cases}
\tag{2.13}
$$

We consider the external magnetic field $\mathbf{h}_{\mathrm{ext}}$ of the following form:

$$
\mathbf{h}_{\mathrm{ext}} = (h_1, h_2, h_3) = h\,(\sin\Theta\cos\Phi,\ \sin\Theta\sin\Phi,\ \cos\Theta)\,,
\tag{2.14}
$$

where Θ, Φ, and h are the inclination angle, azimuthal angle, and strength of the external magnetic field, respectively. The orientation of the external magnetic field can be tuned via the angles Θ and Φ.

Subsequently, the second torque term $\mathbf{t}^{\mathrm{dis}}$ in Eq. (2.1) describes the dissipative processes in the system and is comprised of two distinct components. The first component corresponds to the standard linear Gilbert-dissipation torque, representing energy dissipation in an ideal ferromagnetic material. The second component represents nonlinear rate-independent dry-friction dissipation that arises due to crystallographic defects such as impurities, inhomogeneities, and other metallic deficiencies present in the material (cf. [12,14,21,28,29,42]). It reads as:

$$
\mathbf{t}^{\mathrm{dis}} = \left[\alpha_G + \gamma\alpha_D \left|\frac{\partial \mathbf{m}}{\partial t}\right|^{-1}\right]\left(\mathbf{m}\times\frac{\partial \mathbf{m}}{\partial t}\right),
\tag{2.15}
$$

where the coefficient α_G accounts for the classical Gilbert damping and α_D stands for the dry-friction parameter that measures the average distributions of defects in the material.

Finally, the last torque term presented in Eq. (2.1) delineates the inertial damping due to nutation oscillations and is expressed as (cf. [31–37]):

$$
\mathbf{t}^{\mathrm{iner}} = \alpha_G \tau \left(\mathbf{m}\times\frac{\partial^2 \mathbf{m}}{\partial t^2}\right),
\tag{2.16}
$$

where, $\tau > 0$ denotes the relaxation time for angular momentum. It is characterized by nutation dynamics, which are superimposed magnetization oscillations occurring at a significantly higher frequency than the damped precession dynamics. The parameter τ plays a crucial role in distinguishing between two distinct regimes: the short-time dynamics ($t \approx \tau$) exhibiting nutation oscillations due to inertial term, and the long-time dynamics ($t \gg \tau$) depicting precession oscillations around the applied magnetic field.

Next, to analyze the DW propagation, we employ the polar framework, in which the unitary magnetization vector is defined by the polar angle $\vartheta(x,t)$ and the azimuthal angle $\varphi(x,t)$ as:

$$\mathbf{m}(x,t) = \sin\vartheta\cos\varphi\ \mathbf{e}_1 + \sin\vartheta\sin\varphi\ \mathbf{e}_2 + \cos\vartheta\ \mathbf{e}_3 \tag{2.17}$$

By inserting Eqs. (2.4)-(2.7),(2.15), (2.16) and (2.17) into Eq. (2.1), we obtain:

$$\begin{aligned}
&\sin\vartheta\dot{\varphi} - \left[\alpha_G + \gamma\alpha_D\left(\dot{\vartheta}^2 + \sin^2\vartheta\dot{\varphi}^2\right)^{-1/2}\right]\dot{\vartheta} \\
&\quad = \gamma\left[-A\frac{\partial^2\vartheta}{\partial x^2} + A\sin\vartheta\cos\vartheta\left(\frac{\partial\varphi}{\partial x}\right)^2 - \cos\vartheta\cos\varphi\left(h_1 + h_1^{\mathrm{me}} + h_1^{\mathrm{an}}\right) - \cos\vartheta\sin\varphi\right. \\
&\qquad \left.\times\left(h_2 + h_2^{\mathrm{me}} + h_2^{\mathrm{an}}\right) + \sin\vartheta\left(h_3 + h_3^{\mathrm{me}} + h_3^{\mathrm{an}}\right) + \sin\vartheta\cos\vartheta\left(N_1\cos^2\varphi + N_2\sin^2\varphi - N_3\right)\right] \\
&\qquad + \alpha_G\tau\ \ddot{\vartheta} - \alpha_G\tau\ \sin\vartheta\cos\vartheta\ (\dot{\varphi})^2\,,
\end{aligned} \tag{2.18}$$

$$\begin{aligned}
&\left[\alpha_G + \gamma\alpha_D\left(\dot{\vartheta}^2 + \sin^2\vartheta\dot{\varphi}^2\right)^{-1/2}\right]\sin\vartheta\dot{\varphi} + \dot{\vartheta} \\
&\quad = \gamma\left\{A\sin\vartheta\frac{\partial^2\varphi}{\partial x^2} + 2A\cos\vartheta\frac{\partial\vartheta}{\partial x}\frac{\partial\varphi}{\partial x} + (N_1 - N_2)\sin\vartheta\cos\varphi\sin\varphi + \left(h_2 + h_2^{\mathrm{me}} + h_2^{\mathrm{an}}\right)\cos\varphi\right. \\
&\qquad \left. - \left(h_1 + h_1^{\mathrm{me}} + h_1^{\mathrm{an}}\right)\sin\varphi\right\} - \alpha_G\tau\sin\vartheta\ddot{\varphi} - 2\alpha_G\tau\cos\vartheta\ \dot{\vartheta}\dot{\varphi}\,,
\end{aligned} \tag{2.19}$$

where the components of the magnetocrystalline anisotropy field (2.6) and the magnetoelastic field (2.7) read as:

$$h_1^{\mathrm{an}} = 0 = h_2^{\mathrm{an}}\,,\quad h_3^{\mathrm{an}} = \frac{2K}{\mu_0 M_s^2}\cos\vartheta\ . \tag{2.20}$$

and,

$$\begin{aligned}
h_1^{\mathrm{me}} &= \frac{2}{\mu_0 M_s^2}\sin\theta\cos\varphi\,(\lambda_A - \lambda_B)\left\{\cos^2\theta\left[\left(\lambda_A c_{11} + \lambda_B c_{12} - \frac{c_{13}^2}{c_{33}}(\lambda_A + \lambda_B)\right]\right.\right. \\
&\quad \left.\left. + \left[c_{11}\epsilon_{11} + c_{12}\epsilon_{22} - \frac{c_{13}^2}{c_{33}}(\epsilon_{11} + \epsilon_{22} - \lambda_A - \lambda_B - 2\lambda_{13}) - (\lambda_A + \lambda_{13})\,c_{11} - (\lambda_B + \lambda_{13})\,c_{12}\right]\right\}, \\
h_2^{\mathrm{me}} &= \frac{2}{\mu_0 M_s^2}\sin\theta\sin\varphi\,(\lambda_A - \lambda_B)\left\{\cos^2\theta\left[\left(\lambda_A c_{11} + \lambda_B c_{12} - \frac{c_{13}^2}{c_{33}}(\lambda_A + \lambda_B)\right]\right.\right. \\
&\quad \left.\left. + \left[c_{12}\epsilon_{11} + c_{11}\epsilon_{22} - \frac{c_{13}^2}{c_{33}}(\epsilon_{11} + \epsilon_{22} - \lambda_A - \lambda_B - 2\lambda_{13}) - (\lambda_A + \lambda_{13})\,c_{11} - (\lambda_B + \lambda_{13})\,c_{12}\right]\right\}, \\
h_3^{\mathrm{me}} &= \frac{2}{\mu_0 M_s^2}\cos\theta\lambda_B\left(\frac{2c_{13}^2}{c_{33}} - c_{11} - c_{12}\right)\left\{\epsilon_{11} + \epsilon_{22} - (\lambda_A + \lambda_B + 2\lambda_{13}) + \cos^2\theta\,(\lambda_A + \lambda_B)\right\},
\end{aligned} \tag{2.21}$$

To characterize the DW motion in the steady-state and precessional dynamic regime, we derive the functional dependence of the relevant dynamic quantities on the considered key parameters.

2.1 Steady-state regime

Experimental evidence has revealed a phase transition in DW motion as the strength of external sources (magnetic fields or electric currents) increases. Within a certain range of external fields, the DW profile undergoes a rigid motion with a constant velocity v at a fixed azimuthal angle φ_0 along the major axis $\mathbf{e}_1$ of FMS. This phase is commonly referred to as a steady-state regime. The behavior of the DW in this regime can be described using a mathematical framework known as the traveling wave ansatz, where the polar angle is expressed as $\vartheta = \vartheta(\xi)$, with $\xi = x - vt$ as the spatiotemporal traveling wave variable. According to these assumptions, Eqs. (2.18) and (2.19) reduces to:

$$\begin{aligned}\alpha_G \tau v^2 \vartheta'' - \alpha_G v\, \vartheta' - \widehat{\alpha_D} \;&= \gamma \Big\{ A\vartheta'' + \Big(N_3 - N_2 \sin^2\varphi_0 - N_1 \cos^2\varphi_0\Big) \sin\vartheta\cos\vartheta \\ &\quad - \big(h_3 + h_3^{\mathrm{me}} + h_3^{\mathrm{an}}\big)\sin\vartheta + \big[\big(h_1 + h_1^{\mathrm{me}} + h_1^{\mathrm{an}}\big)\cos\varphi_0 \\ &\quad + \big(h_2 + h_2^{\mathrm{me}} + h_2^{\mathrm{an}}\big)\sin\varphi_0\big]\cos\vartheta \Big\}, \qquad (2.22)\\ v\,\vartheta' \;&= \gamma \Big\{ (N_2 - N_1)\sin\varphi_0\cos\varphi_0\sin\vartheta - \big(h_2 + h_2^{\mathrm{me}} + h_2^{\mathrm{an}}\big)\cos\varphi_0 + \big(h_1 + h_1^{\mathrm{me}} + h_1^{\mathrm{an}}\big)\sin\varphi_0 \Big\}, \qquad (2.23)\end{aligned}$$

where, the prime represents the derivative with respect to the traveling wave variable ξ. Also $\widehat{\alpha_D} = \gamma\alpha_D \operatorname{sign}\big(v\vartheta'\big)$.

The steady-state regime exists when the strength of the external sources falls within the range between the threshold value and the critical WB value. Considering Eqs. (2.14), (2.21) and (2.20), Eq. (2.23) can be recast as:

$$\vartheta' = \Gamma\,(\sin\vartheta + \Upsilon)\,, \qquad (2.24)$$

where,

$$\Gamma = \frac{\gamma}{2v}\left[(N_2 - N_1) - \frac{2}{\mu_0 M_s^2}\,(\lambda_A - \lambda_B)\,(c_{11} - c_{12})\,(\epsilon_{22} - \epsilon_{11})\right]\sin(2\varphi_0)\,, \qquad (2.25)$$

$$\Upsilon = \frac{2\mu_0 M_s^2\;(h_2\cos\varphi_0 - h_1\sin\varphi_0)}{\big[2(\lambda_A - \lambda_B)\,(c_{11} - c_{12})\,(\epsilon_{22} - \epsilon_{11}) - (N_2 - N_1)\,\mu_0 M_s^2\big]\sin(2\varphi_0)}\,. \qquad (2.26)$$

Let us emphasize that $\Upsilon = 0$ corresponds to the external magnetic field aligning along the $\mathbf{e}_3$ direction (i.e., $h_1 = h_2 = 0$). In this case, the solution takes the classical form:

$$\vartheta(\xi) = 2\arctan(e^{\Gamma\xi}) = 2\tan^{-1}\left\{\exp\left(\frac{x - vt}{\delta}\right)\right\}\,. \qquad (2.27)$$

Now, we discuss the solutions obtained as a function of the quantity $|\Upsilon|$. Given our focus on identifying monotonic traveling wave solutions that connect the equilibrium states, we treat Υ as a constant parameter. Under the constraint $|\Upsilon| < 1$, the solutions can be expressed as follows:

$$\vartheta(\xi) = \arccos\left(\frac{1 - F^2(\xi)}{1 + F^2(\xi)}\right), \qquad (2.28)$$

with,

$$F(\xi) = \frac{\eta f_2 \exp(\xi\Gamma) - f_1}{\eta\exp(\xi\Gamma) - 1}, \qquad (2.29)$$

where f_1, f_2, η are constants and Γ^{-1} denotes the DW width. We remark that when $|\Upsilon| \ll 1$, the solution given in Eq. (2.28) takes a form similar to the well-known Walker's type solution (cf. [23,57]).

For $|\Upsilon| > 1$ the solution adopts a following form:

$$\vartheta = 2\arctan\left\{\frac{\sqrt{\Upsilon^2 - 1}\tan\left[\Gamma\sqrt{\Upsilon^2 - 1}\xi + \kappa\right] - 1}{\Upsilon}\right\}, \qquad (2.30)$$

being κ the integration constant,

$$\kappa = \frac{1}{\sqrt{\Upsilon^2 - 1}} \arctan\left(\frac{\Upsilon + 1}{\sqrt{\Upsilon^2 - 1}}\right) \tag{2.31}$$

where κ is chosen so that the variable ϑ evaluated at the center of the DW is null. In this case, the traveling wave solution does not satisfy the Dirichlet boundary conditions. Hence, the solution is only locally valid, namely, in the proximity of the center of the DW (cf. [58]).

Now, taking into account Eqs. (2.14), (2.21), (2.20) and (2.24), Eq. (2.22) recast as:

$$\Lambda_1 \ \sin\vartheta + \Lambda_2 \ \cos\vartheta + \Lambda_3 \ \sin\vartheta\cos\vartheta + \Lambda_4 \ \sin\vartheta\cos^3\vartheta + \Lambda_5 = 0, \tag{2.32}$$

where,

$$\begin{aligned}
\Lambda_1 &= \Gamma\,(\alpha_G v) - \gamma\, h_3, \\
\Lambda_2 &= \gamma\left\{h_1\cos\varphi_0 + h_2\sin\varphi_0 + \left(A - \frac{\alpha_G \tau v^2}{\gamma}\right)\Gamma^2\Upsilon\right\}, \\
\Lambda_3 &= \gamma\left\{\left(A - \frac{\alpha_G \tau v^2}{\gamma}\right)\Gamma^2 + N_3 - N_2\sin^2\varphi_0 - N_1\cos^2\varphi_0 + \frac{2(\psi - K)}{\mu_0 M_s^2}\right\}, \\
\Lambda_4 &= \frac{2\gamma}{\mu_0 M_s^2}\left\{(\lambda_A^2 + \lambda_B^2)c_{11} + 2\lambda_A\lambda_B c_{12} - (\lambda_A + \lambda_B)^2\frac{c_{13}^2}{c_{33}}\right\}, \\
\Lambda_5 &= \Upsilon\,(\alpha_G v)\,\Gamma + \widehat{\alpha_D}\,.
\end{aligned} \tag{2.33}$$

Furthermore, we retrieve the expression for DW width $\delta = 1/\Gamma$ by setting $\Lambda_3 = 0$ (cf. [7,12,21,29,43]), as follows:

$$\delta = \sqrt{\frac{A_{\text{exc}} - \beta}{K - \psi + \frac{1}{2}\mu_0 M_s^2\left(N_1\cos^2\varphi_0 + N_2\sin^2\varphi_0 - N_3\right)}}, \tag{2.34}$$

with,

$$\beta = \frac{\alpha_G \tau \mu_0 M_s^2 v^2}{2\gamma}, \tag{2.35}$$

and,

$$\begin{aligned}
\psi = {} & (\lambda_A - \lambda_B)\Big[\left(c_{11}\cos^2\varphi_0 + c_{12}\sin^2\varphi_0\right)\epsilon_{11} + \left(c_{12}\cos^2\varphi_0 + c_{11}\sin^2\varphi_0\right)\epsilon_{22}\Big] \\
& + \left[\lambda_B\,(c_{11} + c_{12}) - \frac{c_{13}^2}{c_{33}}\,(\lambda_A + \lambda_B)\right](\epsilon_{11} + \epsilon_{22}) + \frac{c_{13}^2}{c_{33}}\,(\lambda_A + \lambda_B + 2\lambda_{13})\,(\lambda_A + \lambda_B) \\
& - \left[\lambda_A^2 + \lambda_B^2 + \lambda_{13}\,(\lambda_A + \lambda_B)\right]c_{11} - \left[2\lambda_A\lambda_B + \lambda_{13}\,(\lambda_A + \lambda_B)\right]c_{12}.
\end{aligned} \tag{2.36}$$

For brevity, we assume:

$$\chi = \left[(N_2 - N_1) - \frac{2}{\mu_0 M_s^2}\,(\lambda_A - \lambda_B)\,(c_{11} - c_{12})\,(\epsilon_{22} - \epsilon_{11})\right] \text{ such that, } \Gamma = \frac{\gamma\chi}{2v}\sin(2\varphi_0) \tag{2.37}$$

and,

$$\rho = K - \psi + \frac{1}{2}\mu_0 M_s^2\left(N_1\cos^2\varphi_0 + N_2\sin^2\varphi_0 - N_3\right) \text{ such that, } \delta = \left(\frac{A_{\text{exc}} - \beta}{\rho}\right)^{1/2}. \tag{2.38}$$

In our analysis, we assume that a 180° Bloch wall is nucleated within the FMS, where magnetization vectors in the opposite domains align themselves along the $\pm\mathbf{e}_3$ axes. This specific configuration is distinguished by $\vartheta(\xi) \simeq 0$ for $\xi \to -\infty$ and $\vartheta(\xi) \simeq \pi$ for $\xi \to +\infty$ which correspond to the boundary conditions established

by the classical Walker solution. Then, computing the average of Eq. (2.32) across the entire domain wall, spanning from the first domain to the second (i.e., $0^\circ \leq \vartheta \leq 180^\circ$), we obtain the expression for the DW velocity within the steady regime as:

$$v = \frac{\sqrt{2\gamma A_{\text{exc}}}\,(2\gamma h\cos\Theta - \pi\widehat{\alpha_D})}{\sqrt{2\gamma\rho\alpha_G^2\,(2+\pi\Upsilon)^2 + \tau\alpha_G\mu_0 M_s^2\,(2\gamma h\cos\Theta - \pi\widehat{\alpha_D})^2}}, \tag{2.39}$$

which is associated with several key factors, including the dry-friction coefficient, magnetostriction, relaxation time for angular momentum, piezo-induced strains, and DW width.

Furthermore, it is essential to emphasize that DW velocities adhere to the constraint $v \geq 0$. Hence, by analyzing Eq. (2.39), we deduce threshold condition of the applied magnetic field $h^{(th)}$:

$$v = 0 \Longrightarrow h^{(\text{th})} = \frac{\pi}{2\gamma\cos\Theta}\widehat{\alpha_D}\,. \tag{2.40}$$

An additional restriction $v \leq v^{(WB)}$ on the DW velocity arises from Eqs. (2.25) and (2.34) and yields the WB limit for the DW velocity:

$$v^{(WB)} = \left(\frac{2\gamma^2\chi^2 A_{\text{exc}}}{8\rho + \gamma\alpha_G\tau\mu_0 M_s^2\chi^2}\right)^{1/2}. \tag{2.41}$$

Also, we deduce the WB limit of applied magnetic field $h^{(WB)}$ using Eqs. (2.39) and (2.41) as:

$$h^{(WB)} = \frac{\pi}{\Delta}\,(\widehat{\alpha_D} + \gamma\alpha_G\chi)\,, \quad \text{where } \Delta = 2\gamma\cos\Theta + \frac{\gamma\pi\alpha_G\sin\Theta\sin(\Phi-\varphi_0)}{\sin(2\varphi_0)}. \tag{2.42}$$

The constraint $0 \leq v \leq v^{(WB)}$ reflects the range of the DW velocity in the steady-state regime.

2.2 Precessional regime

In this section, we explore the dynamics of the precessional regime, which occurs when the breakdown condition is violated. The motion in this phase is characterized by a time-dependent velocity $v(t)$. It exhibits periodic oscillations at microwave frequencies while maintaining a constant angular speed $\dot{\varphi} = \omega_0$. Now, the governing equations (2.18) and (2.19) can be rewritten in the form:

$$\begin{aligned}
&\omega_0\sin\vartheta + \left[\alpha_G v + \gamma\alpha_D v\left(v^2\vartheta'^2 + {\omega_0}^2\sin^2\vartheta\right)^{-1/2}\right]\vartheta' = \gamma\left[-\left(A - \frac{\alpha_G\tau v^2}{\gamma}\right)\vartheta''\right.\\
&-\cos\vartheta\cos\varphi\left(h_1 + h_1^{\text{me}} + h_1^{\text{an}}\right) - \cos\vartheta\sin\varphi\left(h_2 + h_2^{\text{me}} + h_2^{\text{an}}\right) + \sin\vartheta\left(h_3 + h_3^{\text{me}} + h_3^{\text{an}}\right)\\
&\left.+\sin\vartheta\cos\vartheta\left(N_1\cos^2\varphi + N_2\sin^2\varphi - N_3\right)\right] - \alpha_G\tau{\omega_0}^2\,\sin\vartheta\cos\vartheta,
\end{aligned} \tag{2.43}$$

$$\begin{aligned}
&\left[\alpha_G + \gamma\alpha_D\left(\,v^2\vartheta'^2 + {\omega_0}^2\sin^2\vartheta\right)^{-1/2}\right]\sin\vartheta\omega_0 - (v + 2\alpha_G\tau v\omega_0\cos\vartheta)\vartheta'\\
&\qquad = \gamma\left\{(N_1 - N_2)\sin\vartheta\sin\varphi\cos\varphi - \left(h_1 + h_1^{\text{me}} + h_1^{\text{an}}\right)\sin\varphi + \left(h_2 + h_2^{\text{me}} + h_2^{\text{an}}\right)\cos\varphi\right\}.
\end{aligned} \tag{2.44}$$

Assuming that the traveling wave profile given in Eq. (2.24) is unchanged, Eqs. (2.43) and (2.44) can be recast in the following form:

$$\omega_0 + \Gamma(1+\Upsilon)\left[\alpha_G + \gamma\alpha_D\left(v^2\Gamma^2(1+\Upsilon)^2 + \omega_0^2\right)^{-1/2}\right]v = \gamma\; h\cos\Theta, \tag{2.45}$$

$$\begin{aligned}
&\left[\alpha_G + \gamma\alpha_D\left(v^2\Gamma^2(1+\Upsilon)^2 + \omega_0^2\right)^{-1/2}\right]\omega_0 = \Gamma(1+\Upsilon)v + h\sin\Theta\sin(\Phi-\varphi_0)\\
&\qquad + \gamma\sin\varphi_0\cos\varphi_0\left\{N_1 - N_2 + \frac{2}{\mu_0 M_s^2}\,(\lambda_A - \lambda_B)\,(c_{11} - c_{12})\,(\epsilon_{22} - \epsilon_{11})\right\},
\end{aligned} \tag{2.46}$$

where all the quantities have been evaluated at the center of the DW $\left(\vartheta = \frac{\pi}{2}\right)$.

Next, assuming the hypothesis $\Gamma(1+\Upsilon)\bar{v} \ll \omega_0$ and taking the average of Eqs. (2.45) and (2.46) over a period of precession, we obtain:

$$\begin{aligned} \omega_0 + \alpha_G \Gamma(1+\Upsilon)\bar{v} &= \gamma\, h \cos\Theta, \\ \alpha_G \omega_0 + \gamma \alpha_D &= \Gamma(1+\Upsilon)\bar{v}. \end{aligned} \tag{2.47}$$

Now, by solving Eqs. (2.47), we derive the following expression for the average domain wall velocity in the precessional regime:

$$\bar{v} = \frac{\alpha_G \gamma \delta \cos\Theta}{(1+\Upsilon)\left(1+\alpha_G^2\right)}\, h + \frac{\gamma \alpha_D \delta}{(1+\Upsilon)\left(1+\alpha_G^2\right)}\,. \tag{2.48}$$

3 Numerical results

In this section, we demonstrate numerical illustrations based on the analytical results derived in the previous section. To make a qualitative comparison, we assume realistic parameter values of a hexagonal cobalt-based alloy (Pt/Co/Pt) from the literature (cf. [1,7,54,56,59–63]). We consider the dimensions of the FMS as: length $L = 20\,\mu$m, width $w = 700$ nm, and thickness $d = 20$ nm aligned along the $\mathbf{e}_1$, $\mathbf{e}_2$, and $\mathbf{e}_3$ axes, respectively, satisfying the constraint $L \gg w > d$. Material parameter values are summarized in Table 1.

We consider a range of values for the out-of-plane strain ϵ_{33} between -4×10^{-4} and $+10 \times 10^{-4}$ (cf. [1,7]). Furthermore, as suggested in [7], we incorporate dry-friction coefficient (α_D) that depends on the out-of-plane strain (ϵ_{33}) with the relation $\alpha_D = (1 - \nu\epsilon_{33}) \times 10^{-3}$ where $\nu = 500$. Moreover, we consider the PZT5H material as PES, a type of lead zirconate titanate (PZT) ceramic material known for its exceptional piezoelectric properties such as high piezoelectric coefficient, high electromechanical coupling coefficient, and wide temperature range. It is important to highlight that PZT5H optimizes the system response for controlling the properties of domain walls in various configurations when polarized along the major axis (cf. [64,65]).

In Fig. 2, we demonstrate the relationship between DW width (δ) and the out-of-plane strain (ϵ_{33}) for varying the relaxation time for angular momentum (τ). It can be observed from the figure that the piezo strains have a weak influence on DW width. Furthermore, DW width decreases as inertial damping increases, specifically when τ ranges from the sub-picosecond to the sub-nanosecond scale. Also, the inset graph exhibits the variation of DW width in the absence of inertial damping, consistent with recent theoretical and experimental observations (cf. [1,7]).

In Figs. 3a, b we depict the traveling wave profile obtained by fixing the out-of-plane strain and varying τ and vice-versa, respectively. In particular, in Fig. 3a, for a fixed out-of-plane strain, the traveling wave profile approximates the classical Walker solution (i.e., $\vartheta(-\infty) \approx 0$ and $\vartheta(-\infty) \approx \pi$) in the absence of inertial damping ($\tau = 0$). However, as we increase the value of τ, it deviates away from the classical solution. On the other hand, for a fixed τ, the traveling wave profile shows a weak dependence on the out-of-plane strain, as evident from Fig. 3b.

Next, Fig. 4 illustrates the traveling wave profile by systematically varying the orientation of the external magnetic field. When the external field aligns with the $\mathbf{e}_3$ axis, the polar angle ϑ adopts values of 0 and π in

Table 1 Summary of material parameters for hexagonal Co-based magnetostrictive FMS

Quantity	Unit	Value	References	Quantity	Unit	Value	References
λ_A	–	-45×10^{-6}	[7,54,56]	c_{11}	GPa	320	[7,12,63]
λ_B	–	-95×10^{-6}	[7,54,56]	c_{12}	GPa	190	[7,12,63]
λ_C	–	$+110 \times 10^{-6}$	[7,54,56]	c_{13}	GPa	265	[7,12,63]
λ_E	–	-232×10^{-6}	[7,54,56]	c_{33}	GPa	330	[7,12,63]
λ_S	–	-35×10^{-6}	[1,7,12]	c_{44}	GPa	75	[7,59,60]
λ_{13}	–	-580×10^{-6}	[1,7,12]	N_1	–	0.6417	Assumed
λ_{33}	–	1.002×10^{-3}	[1,7,12]	N_2	–	0.0093	Assumed
K	J/m^3	2×10^5	[1,7,12]	N_3	–	0.3490	Assumed
M_s	A/m	1.2971	[1,7,12]	α_G	–	0.01	Assumed
A_{exc}	pJ/m	14	[7,12,61]	φ_0	deg	10	Assumed

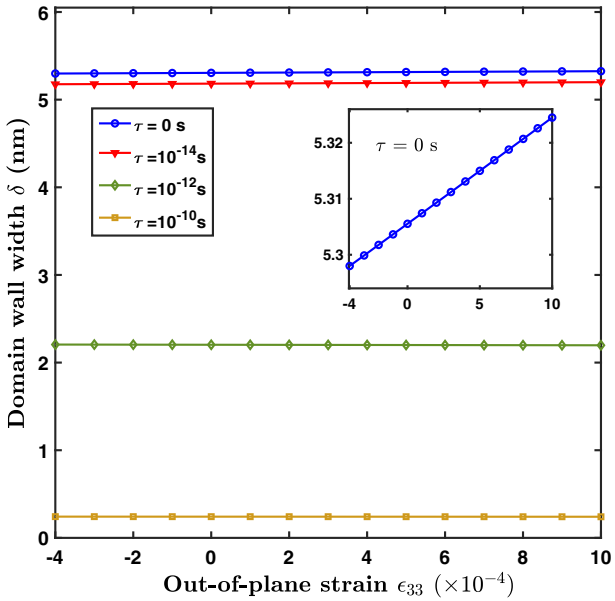

Fig. 2 The dependence of DW width δ on out-of-plane strain ϵ_{33} for varying relaxation time for angular momentum τ

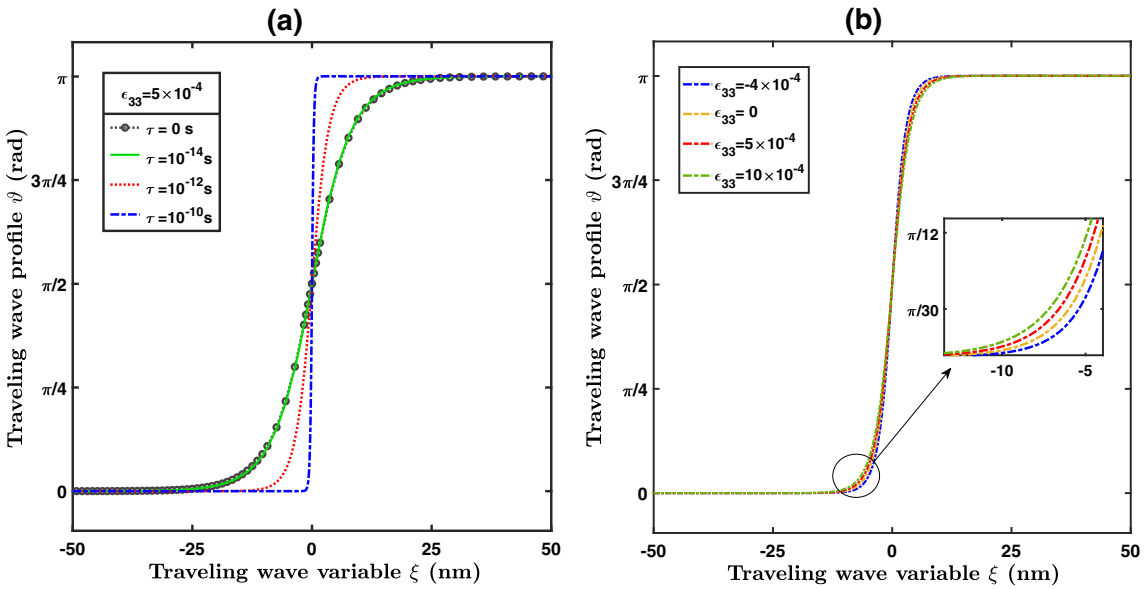

Fig. 3 Comparative analysis of traveling wave profile for **(a)** varying relaxation time for angular momentum τ and fixed out-of-plane strain ϵ_{33}, and **(b)** vice versa

the left and right domains, respectively. It then continuously varies from these values, resembling a traveling wave, as we progress along the positive direction of the strip axis. This behavior corresponds to the classical Walker solution. However, as the orientation of the external magnetic field deviates from the $\mathbf{e}_3$ axis, the DW profile gradually moves away from the classical 180° Bloch wall structure. Moreover, the deviation from the classical Walker profile of the DW structure becomes more significant when the orientation of the external field shifts away from the $\mathbf{e}_3$ axis and inclines towards the $\mathbf{e}_2$ axis.

Furthermore, we examine the boundaries of the steady-state regime for the external magnetic field portrayed in Fig. 5. This investigation is conducted in response to the out-of-plane strain, considering the orientation of the external magnetic field. We illustrate the threshold and the WB values of the external magnetic field in Fig. 5a, b respectively. We observe that the threshold and WB limit of the external magnetic field decreases

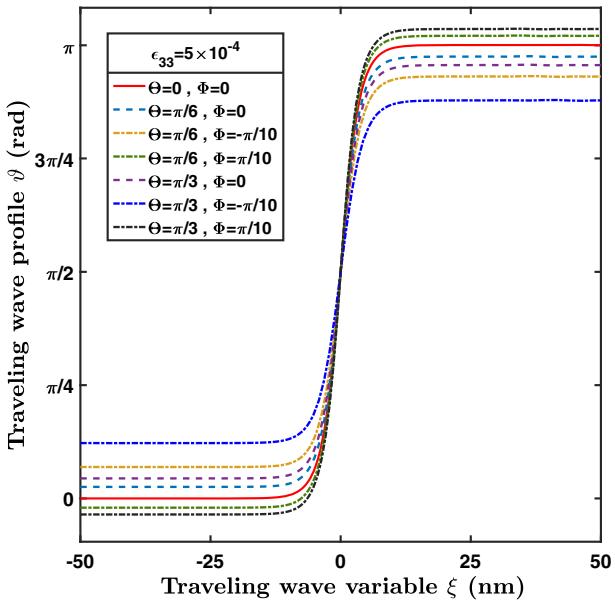

Fig. 4 Traveling wave profile varying external magnetic field orientation for fixed $\tau = 10^{-12}s$

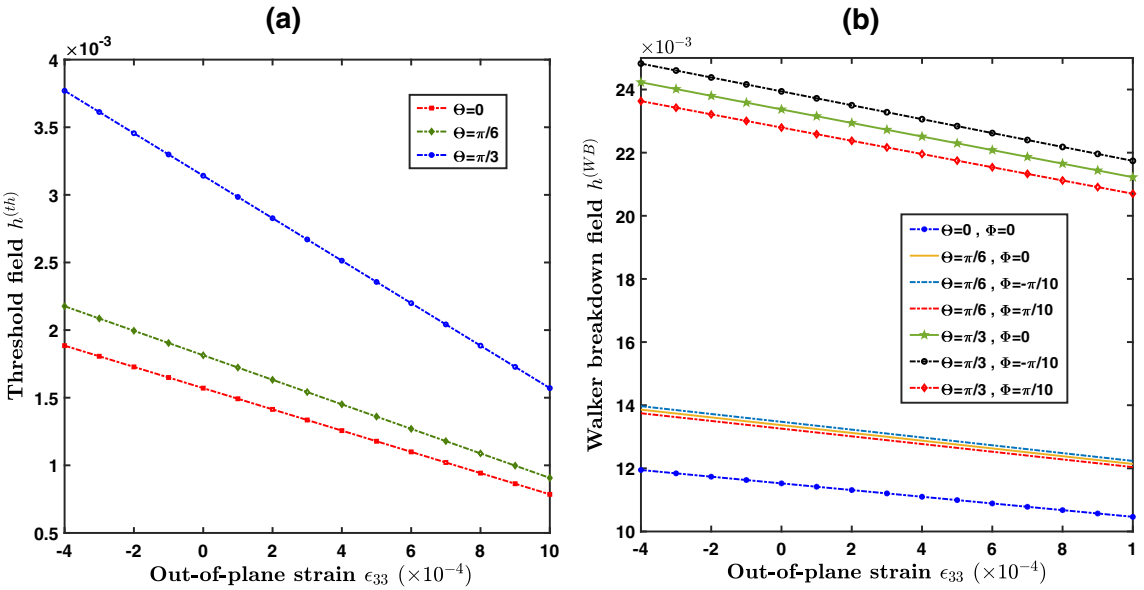

Fig. 5 The variation of **(a)** threshold field $h^{(th)}$, **(b)** Walker breakdown field $h^{(WB)}$ with out-of-plane strain ϵ_{33} varying external field orientation

linearly as we gradually increase the out-of-plane strain. Also, the boundaries of the steady-state regime can be modulated by suitably tuning the orientation of the external magnetic field and piezo-induced strain.

In Fig. 6, we illustrate the variation of the WB limit of DW velocity with the out-of-plane strain, considering different values of τ. It is observed that regardless of the changes in τ, the WB limit of DW velocity experiences a linear decrease with increasing out-of-plane strain. However, the WB value of DW velocity enhanced significantly when τ falls within the sub-picosecond range compared to the sub-nanosecond range.

Furthermore, the dynamic behavior of the steady DW velocity with respect to the external magnetic field is illustrated in Figs. 7 and 8. These figures depict the impact of out-of-plane strain, inertial damping, and the orientation of the external magnetic field on the DW velocity. In particular, Figs. 7a, b show the velocity profile by keeping the out-of-plane strain constant and varying τ and vice-versa, respectively. It is evident from Fig. 7a that the presence of inertial damping leads to a decrease in DW velocity. However, when τ varies

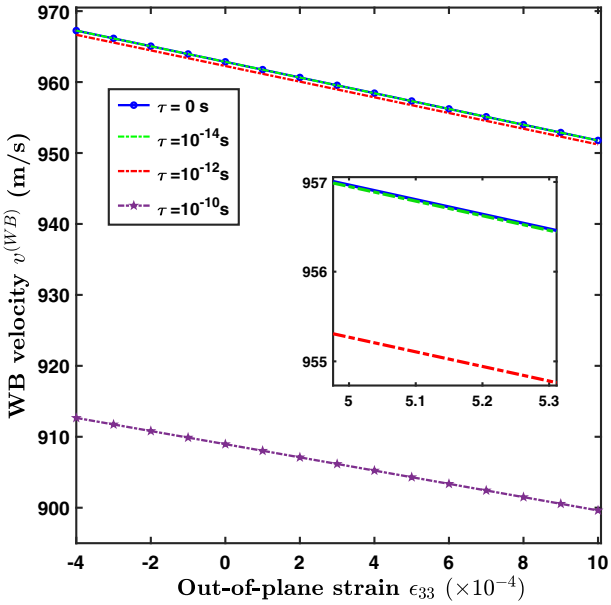

Fig. 6 The variation of Walker breakdown velocity $v^{(WB)}$ with out-of-plane strain ϵ_{33} varying relaxation time for angular momentum τ

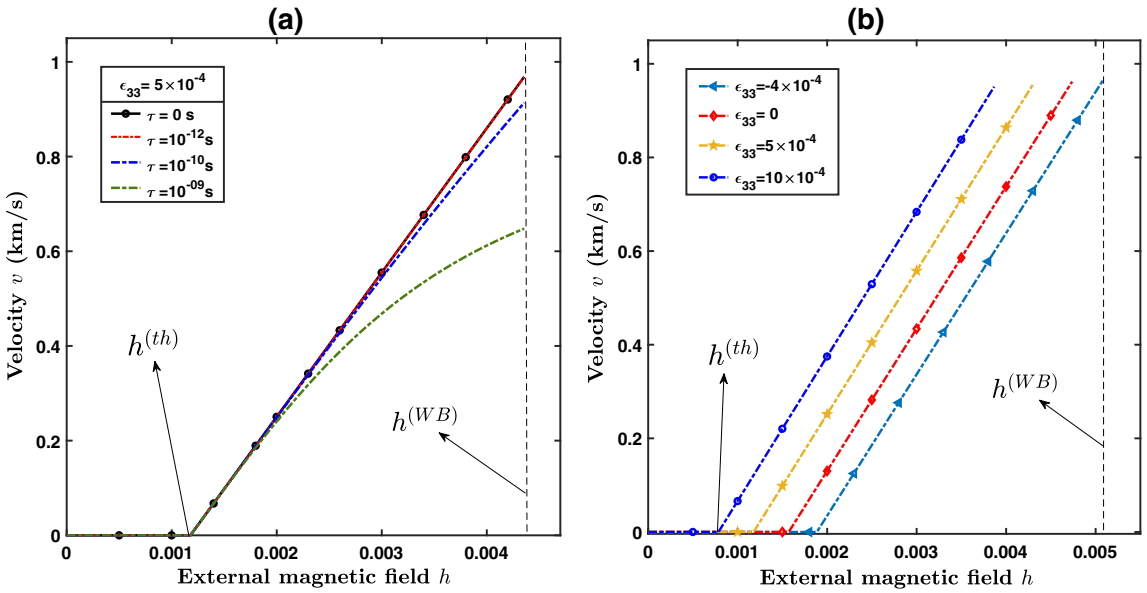

Fig. 7 Comparative analysis of DW velocity varying **(a)** relaxation time for angular momentum τ, **(b)** out-of-plane strain ϵ_{33}

from nanoseconds to picoseconds, DW velocity increases and approaches the value obtained without inertial damping. On the other hand, Fig. 7b demonstrates that higher out-of-plane strain yields higher DW velocity for a fixed external magnetic field. In addition, for a fixed out-of-plane strain, DW velocity increases linearly with the external magnetic field. Moreover, Fig. 8 represents the effect of orientation of the external magnetic field on the DW velocity for the fixed out-of-plane strain and parameter τ. It is evident that for a fixed strength of the external magnetic field, the DW velocity decreases as we slightly deviate from the $\mathbf{e}_3$-direction. However, more deviation from the $\mathbf{e}_3$-axis (i.e., $\Theta = \pi/3$) results in the expansion of the steady-state regime.

Finally, we demonstrate the DW motion in the precessional dynamic regime by considering the variation of inertial damping parameter, out-of-plane strain, and the orientation of the external magnetic field, as depicted in Figs. 9 and 10. It is worth mentioning that an increase in the inertial damping parameter resulted in a reasonable decrease in the average DW velocity, as demonstrated in Fig. 9a. Furthermore, it can be argued

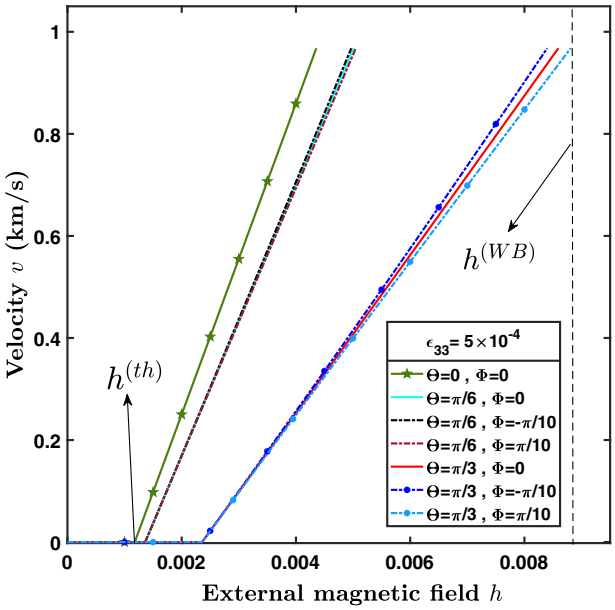

Fig. 8 The variation of DW velocity with external field orientation for $\tau = 10^{-12}s$

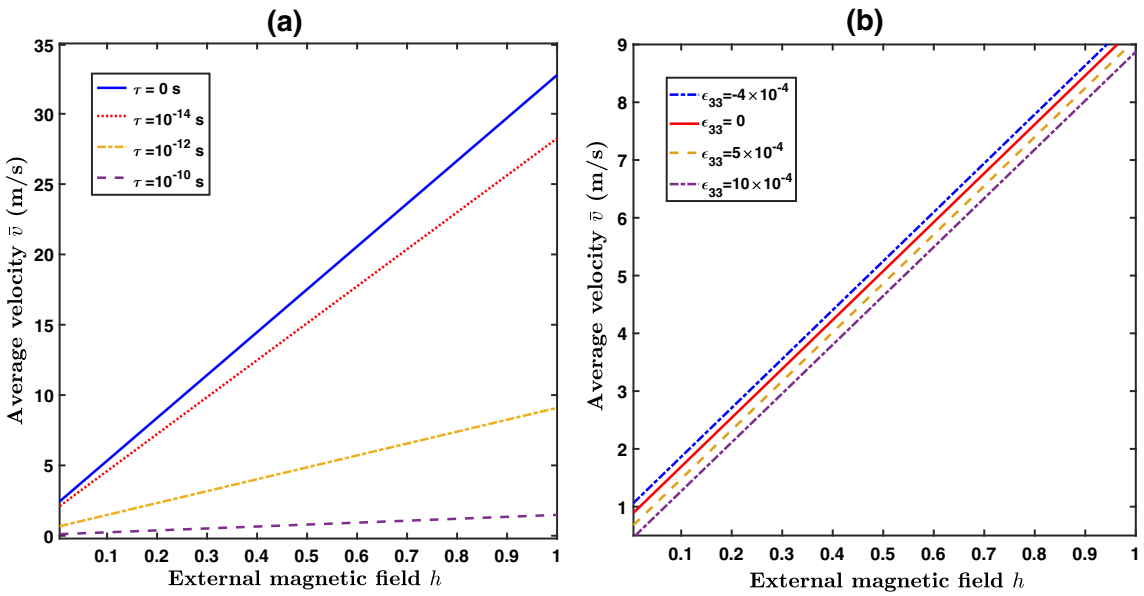

Fig. 9 Comparative analysis of average DW velocity with external magnetic field varying **(a)** relaxation time for angular momentum, **(b)** out-of-plane strain in the precessional regime

from Fig. 9b that the average DW velocity shifts upward as the external magnetic field increases. It is noticed that a lower out-of-plane strain corresponds to a higher average velocity. Lastly, Fig. 10 vividly illustrates that the modulus of the average DW velocity exhibits a linear increase with the external magnetic field. Moreover, for a small magnetic field (up to some critical value), the average DW velocity is higher for the case when the orientation of the external magnetic field deviates more from the $\mathbf{e}_3$ direction. On the other hand, as the strength of the external magnetic field exceeds the critical value, the behavior of the average DW velocity is reversed.

Now, we compare the sole influence of inertial effects on the DW velocity to the works reported in the literature (cf. [1,7,12,31,38]). In particular, the works presented in [7,12] examine the strain-controlled dynamics of a 180° Bloch DW in a bilayer piezoelectric-magnetostrictive heterostructure of the hexagonal

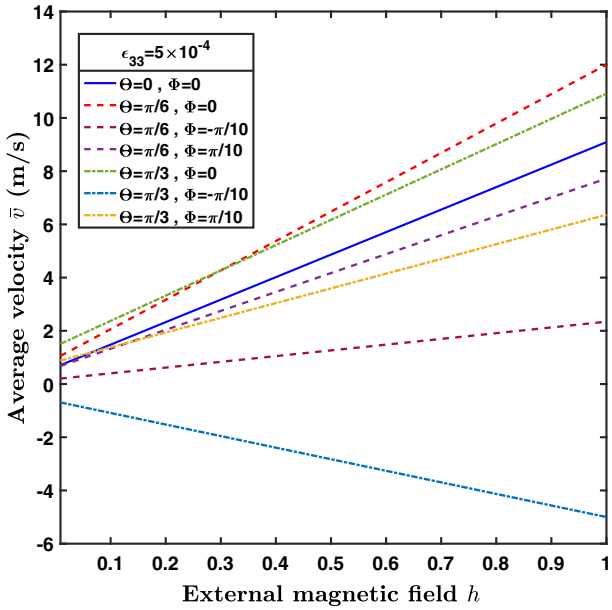

Fig. 10 The variation of average velocity $\bar{v}$ with magnetic field strength varying external magnetic field orientation when $\tau = 10^{-12}s$

crystal class, taking into account magnetostriction, dry friction, and Rashba effects. In these studies, the external magnetic field is applied in a particular direction perpendicular to the plane, which drives the DW's motion. The DW velocity increases linearly with the applied magnetic field under dry-friction and magnetoelastic effects. We observe similar behaviour without inertial damping, which aligns well with these studies in steady-state and precessional regimes (cf. [1,7,12]). Moreover, the works discussed in ([31,38]) investigate the effects of inertial damping on the DW dynamics in ferromagnetic materials. These studies reveal nonlinearity in the DW velocity with the external field under the influence of inertial damping. A similar trend for the DW velocity caused by the inertial damping is also observed in our analysis.

In summary, this investigation delineates that the strain-induced DW motion within hexagonal magnetostrictive material, as considered in the FMS-PES bilayer composite structure, can be controlled by suitably tuning the key parameters: piezo-induced strains, applied magnetic field, and inertial damping.

At this junction, we remark that the results presented herein give valuable insights, such as the dependence of DW width on the inertial damping parameter. Moreover, DW velocity can be effectively manipulated via an external magnetic field, inertial damping, and piezo-induced strains in both dynamical regimes. Also, the orientation of the external magnetic field emerges as a key factor that provides an additional degree of freedom to modify the threshold and WB limits.

4 Conclusions

In this study, we theoretically investigated the dynamics of strain-mediated DW propagation under the simultaneous action of an external magnetic field, magnetoelastic field, inertial damping, and nonlinear dissipative effects considering the crystal symmetry of the material. The study is characterized by assuming that the ferromagnetic material is transversely isotropic and belongs to the hexagonal crystal class, FMS is linearly elastic, and the dry-friction coefficient exhibits a linear relationship with the applied strain. The piezo-induced strains are spatially uniform and completely transferred to FMS. Furthermore, the study has comprehensively examined the influence of magnetic field orientation on the system's dynamics. The main conclusions of our investigation are as follows:

1. DW width exhibits negligible dependence on piezo-strains. However, a substantial decrease in width becomes evident as the relaxation time for angular momentum (τ) increases.

2. An increase in inertial damping and out-of-plane strain leads to a deviation of the traveling wave profile from the classical solution. In contrast, a tunable magnetic field significantly influences the classical wall structure.
3. The threshold and WB values of the external magnetic field depend on its orientation and the out-of-plane strain. To be precise, it decreases as the out-of-plane strain increases and the orientation of the external magnetic field deviates from the $\mathbf{e}_3$ direction.
4. The WB limit of DW velocity decreases linearly with increasing out-of-plane strain. However, it is higher when τ falls within the sub-picosecond range compared to the sub-nanosecond range.
5. DW velocity decreases as τ increases, emphasizing the influence of inertial damping on DW dynamics. Moreover, as τ varies from sub-nanoseconds to picoseconds, it gradually increases and approaches the velocity observed without inertial damping.
6. DW velocity decreases as we increase the out-of-plane strain. Also, it can be manipulated by suitably adjusting the direction and strength of the external magnetic field.
7. In the precessional dynamic regime, an increase in the inertial damping parameter yields a decrease in the average DW velocity. Also, it increases linearly with an increase in the external magnetic field.

Finally, we emphasize that our results align well with the observations reported in the existing literature (cf. [1,7,12,31,38]), where previous studies have separately examined the effects of the parameters (inertial damping, tunable magnetic field, stress-free magnetostrictive strains, and crystal symmetry) considered in the present investigation. Also, it is worth mentioning that by applying uniform stress generated by a piezoelectric substrate to a two-domain system, the DW moves to expand the energetically favoured domain and contract the other. It has been reported that stress-mediated control of magnetization offers excellent energy efficiency, presenting a relevant alternative to current/magnetic field-based DW motion techniques, which are subject to higher energy consumption (cf. [47,49,66–69]). We intend to include such aspects in future extensions of our work.

Funding Sharad Dwivedi would like to thank the Science and Engineering Research Board (SERB), Department of Science and Technology, Government of India, and the National Institute of Technology Andhra Pradesh for the financial support through Projects CRG/2019/003101 and NITAP/SDG/15/2020, respectively.

Declarations

Conflict of Interest The authors have no conflicts to disclose.

References

1. Shepley, P.M., Rushforth, A.W., Wang, M., Burnell, G., Moore, T.A.: Modification of perpendicular magnetic anisotropy and domain wall velocity in Pt/Co/Pt by voltage-induced strain. Sci. Rep. **5**(1), 7921 (2015)
2. Miron, I.M., Moore, T., Szambolics, H., Buda-Prejbeanu, L.D., Auffret, S., Rodmacq, B., ... Gaudin, G.: Fast current-induced domain-wall motion controlled by the Rashba effect. Nat. Mater. **10**(6), 419–423 (2011)
3. Wang, K.L., Alzate, J.G., Amiri, P.K.: Low-power non-volatile spintronic memory: STT-RAM and beyond. J. Phys. D Appl. Phys. **46**(7), 074003 (2013)
4. Eerenstein, W., Mathur, N.D., Scott, J.F.: Multiferroic and magnetoelectric materials. Nature **442**(7104), 759–765 (2006)
5. Ryu, K.S., Thomas, L., Yang, S.H., Parkin, S.: Chiral spin torque at magnetic domain walls. Nat. Nanotechnol. **8**(7), 527–533 (2013)
6. Emori, S., Bauer, U., Ahn, S.M., Martinez, E., Beach, G.S.: Current-driven dynamics of chiral ferromagnetic domain walls. Nat. Mater. **12**(7), 611–616 (2013)
7. Consolo, G., Federico, S., Valenti, G.: Magnetostriction in transversely isotropic hexagonal crystals. Phys. Rev. B **101**(1), 014405 (2020)
8. Boona, S.R., Watzman, S.J., Heremans, J.P.: Research Update: utilizing magnetization dynamics in solid-state thermal energy conversion. APL Mater. **4**(10), 360 (2016)
9. Vaz, C.A., Hoffman, J., Ahn, C.H., Ramesh, R.: Magnetoelectric coupling effects in multiferroic complex oxide composite structures. Adv. Mater. **22**(26–27), 2900–2918 (2010)
10. Dwivedi, S., Dubey, S.: On dynamics of current-induced static wall profiles in ferromagnetic nanowires governed by the Rashba field. Int. J. Appl. Comput. Math. **3**, 27–42 (2017)
11. Schryer, N.L., Walker, L.R.: The motion of 180 domain walls in uniform dc magnetic fields. J. Appl. Phys. **45**(12), 5406–5421 (1974)

12. Maity, S., Dolui, S., Dwivedi, S.: Strain-induced fast domain wall motion in hybrid piezoelectric-magnetostrictive structures with Rashba and nonlinear dissipative effects. Acta. Mech. Sin. **40**(9), 423613 (2024)
13. Hubert, A., Schäfer, R.: Magnetic Domains: The Analysis of Magnetic Microstructures. Springer, Berlin (2008)
14. Consolo, G., Federico, S., Valenti, G.: Strain-mediated propagation of magnetic domain-walls in cubic magnetostrictive materials. Ricerche Mat. **70**(1), 81–97 (2021)
15. Chikazumi, S., Graham, C.D.: Physics of Ferromagnetism. Oxford University Press, Oxford (1997)
16. Cullity, B.D., Graham, C.D.: Introduction to Magnetic Materials. Wiley, New York (2011)
17. Clark, A.E., Hathaway, K.B., Wun-Fogle, M., Restorff, J.B., Lograsso, T.A., Keppens, V.M., ... Taylor, R.A.: Extraordinary magnetoelasticity and lattice softening in bcc Fe-Ga alloys. J. Appl. Phys. **93**(10), 8621–8623 (2003)
18. Wuttig, M., Dai, L., Cullen, J.: Elasticity and magnetoelasticity of Fe-Ga solid solutions. Appl. Phys. Lett. **80**(7), 1135–1137 (2002)
19. Rafique, S., Cullen, J.R., Wuttig, M., Cui, J.: Magnetic anisotropy of FeGa alloys. J. Appl. Phys. **95**(11), 6939–6941 (2004)
20. Gopman, D.B., Sampath, V., Ahmad, H., Bandyopadhyay, S., Atulasimha, J.: Static and dynamic magnetic properties of sputtered Fe-Ga thin films. IEEE Trans. Magn. **53**(11), 1–4 (2017)
21. Consolo, G., Valenti, G.: Analytical solution of the strain-controlled magnetic domain wall motion in bilayer piezoelectric/magnetostrictive nanostructures. J. Appl. Phys. **121**(4), 536 (2017)
22. De Ranieri, E., Roy, P.E., Fang, D., Vehsthedt, E.K., Irvine, A.C., Heiss, D., ... Wunderlich, J.: Piezoelectric control of the mobility of a domain wall driven by adiabatic and non-adiabatic torques. Nat. Mater. **12**(9), 808–814 (2013)
23. Consolo, G., Curro, C., Martinez, E., Valenti, G.: Mathematical modeling and numerical simulation of domain wall motion in magnetic nanostrips with crystallographic defects. Appl. Math. Model. **36**(10), 4876–4886 (2012)
24. Mougin, A., Cormier, M., Adam, J.P., Metaxas, P.J., Ferré, J.: Domain wall mobility, stability and Walker breakdown in magnetic nanowires. Europhys. Lett. **78**(5), 57007 (2007)
25. Dwivedi, S., Dubey, S.: Field-driven magnetization reversal in a three-dimensional network of ferromagnetic ellipsoidal samples. Rendiconti del Circolo Matematico di Palermo Series 2, **69**(2), 497–519 (2020)
26. Landau, L. A. L. E., & Lifshitz, E.: On the theory of the dispersion of magnetic permeability in ferromagnetic bodies. In: Perspectives in Theoretical Physics, pp. 51-65. Pergamon (1992)
27. Visintin, A.: Modified Landau-Lifshitz equation for ferromagnetism. Physica B **233**(4), 365–369 (1997)
28. Shahu, C.K., Dwivedi, S., Dubey, S.: Curved domain walls in the ferromagnetic nanostructures with Rashba and nonlinear dissipative effects. Appl. Math. Comput. **420**, 126894 (2022)
29. Maity, S., Dolui, S., Dwivedi, S., Consolo, G.: Domain wall dynamics in cubic magnetostrictive materials subject to Rashba effect and nonlinear dissipation. Z. Angew. Math. Phys. **74**(1), 23 (2023)
30. Consolo, G., Valenti, G.: Traveling wave solutions of the one-dimensional extended Landau-Lifshitz-Gilbert equation with nonlinear dry and viscous dissipations. Acta Appl. Math. **122**, 141–152 (2012)
31. Shahu, C.K., Dwivedi, S., Dubey, S.: Dynamics of curved domain walls in hard ferromagnets with nonlinear dissipative and inertial effects. Physica D **448**, 133737 (2023)
32. Ciornei, M.C., Rubí, J.M., Wegrowe, J.E.: Magnetization dynamics in the inertial regime: nutation predicted at short time scales. Phys. Rev. B **83**(2), 020410 (2011)
33. Wegrowe, J.E., Ciornei, M.C.: Magnetization dynamics, gyromagnetic relation, and inertial effects. Am. J. Phys. **80**(7), 607–611 (2012)
34. Olive, E., Lansac, Y., Wegrowe, J.E.: Beyond ferromagnetic resonance: the inertial regime of the magnetization. Appl. Phys. Lett. **100**(19), 63 (2012)
35. Fähnle, M., Steiauf, D., Illg, C.: Generalized Gilbert equation including inertial damping: derivation from an extended breathing Fermi surface model. Phys. Rev. B **84**(17), 172403 (2011)
36. Neeraj, K., Pancaldi, M., Scalera, V., Perna, S., d'Aquino, M., Serpico, C., Bonetti, S.: Magnetization switching in the inertial regime. Phys. Rev. B **105**(5), 054415 (2022)
37. Neeraj, K., Awari, N., Kovalev, S., Polley, D., Zhou Hagström, N., Arekapudi, S.S.P.K., ... Bonetti, S.: Inertial spin dynamics in ferromagnets. Nat. Phys. **17**(2), 245–250 (2021)
38. Dwivedi, S., Dubey, S.: Field-driven motion of ferrofluids in ferromagnetic nanowire under the influence of inertial effects. Proc. Eng. **127**, 3–9 (2015)
39. Kimel, A.V., Ivanov, B.A., Pisarev, R.V., Usachev, P.A., Kirilyuk, A., Rasing, T.: Inertia-driven spin switching in antiferromagnets. Nat. Phys. **5**(10), 727–731 (2009)
40. Giordano, S., Déjardin, P.M.: Derivation of magnetic inertial effects from the classical mechanics of a circular current loop. Phys. Rev. B **102**(21), 214406 (2020)
41. Dwivedi, S., Singh, Y.P., Consolo, G.: On the statics and dynamics of transverse domain walls in bilayer piezoelectric-magnetostrictive nanostructures. Appl. Math. Model. **83**, 13–29 (2020)
42. Shahu, C.K., Dubey, S., Dwivedi, S.: Domain wall motion in multiferroic nanostructures under the influence of spin-orbit torque and nonlinear dissipative effect. Mech. Adv. Mater. Struct. **5**, 1–11 (2022)
43. Consolo, G.: Modeling magnetic domain-wall evolution in trilayers with structural inversion asymmetry. Ricerche Mat. **67**, 1001–1015 (2018)
44. Moon, K.W., Kim, D.H., Kim, C., Kim, D.Y., Choe, S.B., Hwang, C.: Domain wall motion driven by an oscillating magnetic field. J. Phys. D Appl. Phys. **50**(12), 125003 (2017)
45. Olive, E., Lansac, Y., Meyer, M., Hayoun, M., Wegrowe, J.E.: Deviation from the Landau-Lifshitz-Gilbert equation in the inertial regime of the magnetization. J. Appl. Phys. **117**(21), 523 (2015)
46. Dubey, S., Dwivedi, S.: On controllability of a two-dimensional network of ferromagnetic ellipsoidal samples. Diff. Equ. Dynam. Syst. **27**, 277–297 (2019)
47. Mathurin, T., Giordano, S., Dusch, Y., Tiercelin, N., Pernod, P., Preobrazhensky, V.: Stress-mediated magnetoelectric control of ferromagnetic domain wall position in multiferroic heterostructures. Appl. Phys. Lett. **108**(8), 52 (2016)
48. Dwivedi, S., Dubey, S.: On the stability of steady-states of a two-dimensional system of ferromagnetic nanowires. J. Appl. Anal. **23**(2), 89–100 (2017)

49. Mathurin, T., Giordano, S., Dusch, Y., Tiercelin, N., Pernod, P., Preobrazhensky, V.: Domain-wall dynamics in magnetoelastic nanostripes. Phys. Rev. B **95**(14), 140405 (2017)
50. Ravaud, R., Lemarquand, G.: Magnetic field produced by a parallelepipedic magnet of various and uniform polarization. Prog. Electromag. Res. **98**, 207 (2009)
51. Mathurin, T., Giordano, S., Dusch, Y., Tiercelin, N., Pernod, P., Preobrazhensky, V.: Mechanically driven domain wall movement in magnetoelastic nanomagnets. Eur. Phys. J. B **89**(7), 169 (2016)
52. Sharipov, M.Z., Hayitov, D.E., Raupova, I.B., Sadikova, M.I.: Influence of hexagonal symmetry stresses on domain structure and magnetization process of FeBO3 single crystal. Eurasian Phys. Technol. J. **17**(33), 65–72 (2020)
53. Federico, S., Consolo, G., Valenti, G.: Tensor representation of magnetostriction for all crystal classes. Math. Mech. Solids **24**(9), 2814–2843 (2019)
54. Bozorth, R.M.: Magnetostriction and crystal anisotropy of single crystals of hexagonal cobalt. Phys. Rev. **96**(2), 311 (1954)
55. Mason, W.P.: Derivation of magnetostriction and anisotropic energies for hexagonal, tetragonal, and orthorhombic crystals. Phys. Rev. **96**(2), 302 (1954)
56. Hubert, A., Unger, W., Kranz, J.: Measurement of the magnetostriction constants of cobalt as a function of temperature. Z. Phys. **224**, 148–155 (1969)
57. Podio-Guidugli, P., Tomassetti, G.: On the steady motions of a flat domain wall in a ferromagnet. Eur. Phys. J. B-Conden. Matter Comp. Syst. **26**, 191–198 (2002)
58. Puliafito, V., Consolo, G.: On the travelling wave solution for the current-driven steady domain wall motion in magnetic nanostrips under the influence of Rashba field. Adv. Conden. Matter Phys. **5**, 63 (2012)
59. Bruno, P.: Magnetic surface anisotropy of cobalt and surface roughness effects within Neel's model. J. Phys. F Met. Phys. **18**(6), 1291 (1988)
60. Paes, V.Z.C., Mosca, D.H.: Field-induced lattice deformation contribution to the magnetic anisotropy. J. Appl. Phys. **112**(10), 536 (2012)
61. Eyrich, C., Huttema, W., Arora, M., Montoya, E., Rashidi, F., Burrowes, C., Kardasz, B., Girt, E., Heinrich, B., Mryasov, O.N., From, M., Karis, O.: Exchange stiffness in thin film Co alloys. J. Appl. Phys. **111**(7), 07C919 (2012)
62. Oogane, M., Wakitani, T., Yakata, S., Yilgin, R., Ando, Y., Sakuma, A., Miyazaki, T.: Magnetic damping in ferromagnetic thin films. Jpn. J. Appl. Phys. **45**(5R), 3889 (2006)
63. Nakamura, N., Ogi, H., Hirao, M., Ono, T.: Elastic constants and magnetic anisotropy of Co/Pt superlattice thin films. Appl. Phys. Lett. **86**(11), 563 (2005)
64. Consolo, G., & Valenti, G.: Optimized voltage-induced control of magnetic domain-wall propagation in hybrid piezoelectric/magnetostrictive devices. In: Actuators, Vol. 10, No. 6, p. 134. MDPI (2021)
65. Tang, E., Wang, Y., Wang, R., Han, Y., Chang, M., Chen, C., ... He, L.: Electrical output performance of PZT-5H under the superposition of temperature, temperature change rate and pulse stress. Mater. Chem. Phys. **307**, 128109 (2023)
66. Dean, J., Bryan, M.T., Schrefl, T., Allwood, D.A.: Stress-based control of magnetic nanowire domain walls in artificial multiferroic systems. J. Appl. Phys. **109**(2), 63 (2011)
67. Metaxas, P.J., Sampaio, J., Chanthbouala, A., Matsumoto, R., Anane, A., Fert, A., ... Grollier, J.: High domain wall velocities via spin transfer torque using vertical current injection. Sci. Rep. **3**(1), 1829 (2013)
68. Hu, J.M., Yang, T., Momeni, K., Cheng, X., Chen, L., Lei, S., ... Chen, L.Q.: Fast magnetic domain-wall motion in a ring-shaped nanowire driven by a voltage. Nano Lett. **16**(4), 2341–2348 (2016)
69. Franken, J.H., Yin, Y., Schellekens, A.J., van den Brink, A., Swagten, H.J.M., Koopmans, B.: Voltage-gated pinning in a magnetic domain-wall conduit. Appl. Phys. Lett. **103**(10), 210 (2013)